Modeling nanoscale V-shaped antennas for the design of optical phased arrays

Romain Blanchard, Guillaume Aoust, Patrice Genevet, Nanfang Yu, Mikhail A. Kats, Zeno Gaburro, and Federico Capasso

Phys. Rev. B **85**, 155457 — Published 30 April 2012

DOI: 10.1103/PhysRevB.85.155457

Modeling nanoscale V-shaped antennas for the design of optical phased arrays

Romain Blanchard[1], Guillaume Aoust[1,2], Patrice Genevet[1], Nanfang Yu[1], Mikhail A. Kats[1], Zeno Gaburro[1,3] and Federico Capasso[1]
[1] *School of Engineering and Applied Sciences, Harvard University, Cambridge, MA, USA*
[2] *Ecole Polytechnique, Palaiseau, France*
[3] *Dipartimento di Fisica, Università degli Studi di Trento, Trento, Italy*
(Dated: April 2, 2012)

We present a simplified numerical method to solve for the current distribution in a V-shaped antenna excited by an electric field with arbitrary polarization. The scattered far-field amplitude, phase and polarization of the antennas are extracted. The calculation technique presented here is an efficient method for probing the large design parameter-space of such antennas, which have been proposed as basic building blocks for the design of ultrathin plasmonic metasurfaces. Our calculation is based on the Integral Equation Method of Moments and is validated by comparison to the results of finite-difference time-domain (FDTD) simulations. The computation time is approximately five orders of magnitude less than for FDTD simulations. This speed-up relies mainly on the use of the thin wire approximation whose domain of validity is discussed. This method can be generalized to more complex geometries such as zigzag antennas.

PACS numbers: 00.00.00

I. INTRODUCTION

Optical devices modify the wavefront of light by acting on its phase and amplitude. At the core of many optical components is a spatially varying phase response, as illustrated by a simple lens, which has a parabolic phase profile. Most conventional optical components rely on light propagation over different optical lengths in order to create such a spatial phase response profile. However, it was recently shown[1] that abrupt phase changes over the scale of a wavelength can be introduced by using the phase response of plasmonic resonators. While a single resonator is limited to providing a phase response with a maximum range of π, it was shown that an element consisting of two orthogonal resonators can provide arbitrary amplitude and phase response, covering the entire 2π range for the scattered light component polarized perpendicularly to the incident light[1].

In previous works[1,2], nanoscale gold V-shaped plasmonic antennas supporting two plasmonic eigenmodes of opposite symmetry (Fig. 1 (a)-(b)), and thus acting as two-oscillator systems, were used to provide adequate phase and amplitude control of light. Such V-shaped antennas can be used as the basic building blocks of a new class of flat optical components using phase discontinuities[1–3], since they enable the creation of arbitrary phase and amplitude masks with subwavelength 'pixel' size.

We present here the results of numerical solutions for the current distribution and scattered fields of V-shaped antennas, and in doing so obtain a detailed picture of their near- and far-field properties. In particular, we are able to accurately map their amplitude, phase and polarization responses in arbitrary directions. The convenient modeling tool presented here enables one to select and assemble various V-shaped antennas into more complex optical systems, in addition to giving detailed insight into the behavior of the antenna, illustrating for example the effects of near-field coupling between the two arms.

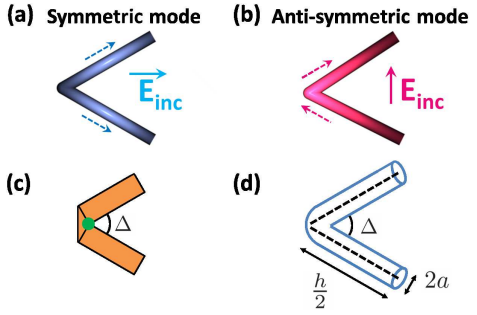

FIG. 1. (a) and (b) Schematic of the first-order (a) symmetric and (b) anti-symmetric modes supported by a V-shaped antenna excited by an incident electric field polarized either (a) along the antenna symmetry axis or (b) perpendicular to the antenna symmetry axis. The arrows indicate the instantaneous direction of the current in each arm while the colored shading represents qualitatively charge density (the darker the more charges). (c) Schematic of a geometry used for FDTD simulations with $h = 1.2$ μm and $\Delta = 60°$. The rectangular arms are 200 nm wide and 100 nm thick. Antennas with different opening angle Δ are obtained by rotation about the connecting corners of the rectangular arms (green dot). The junction is formed by adding a triangular section. (d) Schematic of the geometry used for the Method of Moments calculations. Each antenna arm is modelled as a cylinder of diameter $2a$, but the geometry will be effectively reduced to that of a wire antenna (dashed line). The V-shaped antennas have an opening angle Δ and a total length h.

II. METHOD AND APPROXIMATIONS

Models describing the response of antennas have been extensively studied[4–7]. One of the main challenges is that the integral equations governing the behavior of antennas have no exact analytical solutions. However, with the development of numerical methods in the last few decades, we can obtain accurate numerical solutions in an efficient manner. This work is presenting how the Integral Equation Method of Moments (MoM)[6–10] can be used to study the behavior of V-shaped plasmonic antennas described by a Pocklington-type integral equation[11]. This numerical technique is very general and has been used to compute the characteristics of complex radio-frequency and microwave antenna geometries[6]. The Pocklington equation is often used to determine the current distribution on cylindrical wires of small radius[5–7].

We study here how the methods and approximations used for long-wavelengths apply to the mid-infrared spectral range, where plasmonic properties play a significant role, by comparing our numerical results with the results of finite-difference time-domain (FDTD) simulations. We emphasize that we use a series of approximations to simplify the calculations as much as possible, effectively reducing the problem to one dimension. While full three-dimensional MoM simulation techniques could be implemented on our geometry, our main goal here was to propose a fast and efficient simulation method to probe a large design parameter space, bringing in the meantime radio-frequency methods to the attention of the plasmonics community. Since our numerical solution is one dimensional, it gives direct access to integral quantities such as the current distribution on the antenna, enabling straightforward interpretation of nanoantennas as circuit elements[12–14]. In contrast, three-dimensional FDTD simulations give access to a current density, whose integration into a one-dimensional quantity can be challenging, in particular at corners and edges. Finally, our method is approximately five orders of magnitude faster than FDTD simulations, enabling the accurate mapping of the properties of V-antennas over various geometric parameters.

The geometry considered is that of gold V-shaped antennas fabricated at the interface between a silicon substrate and air. Light is incident on the antenna from the silicon substrate. The antennas are 200 nm wide and 100 nm thick. For all the results presented, the incident wavelength is $\lambda_0 = 7.7$ μm. The two arms of the antennas have equal length ($h/2$), in order to preserve the symmetry of the structure and thus simplify the understanding of the two orthogonal plasmonic modes. We note however that the calculation presented here could very easily be generalized to non-symmetric geometries. As shown in Fig. 1 (c), antennas with different opening angles are obtained by rotation of the rectangular arms about their connecting corners. While this exact geometry is simulated in our FDTD calculations, we use several approximations in our MoM calculations (see Fig. 1 (d)): (1) We assume the antennas to be cylindrical with a radius $a = 100$ nm. The optical properties of the antennas are moderately affected by the cross-section dimensions since they are much smaller than the length of the antenna. We verified that our results have limited dependence on the value of a chosen. (2) We use the thin-wire approximation ($a << \lambda$ and $a << h$, with a the antenna radius and h its total length) which enables us to consider the current distribution on the antenna to be purely axial and azimuthally invariant[6,7], i.e. invariant for rotations around the antenna axis (see Appendix). This approximation transforms the geometry studied to that of an infinitely thin antenna and thus enables to reduce the problem to an effective one-dimensional problem, which results in the dramatic increase observed for the computation speed. Information on the finite dimension of the cross section (radius a) is however preserved in our equations, in particular in the expression of the effective distance between two points of the antenna (see Appendix). While fully justified at long wavelengths, this approximation may seem crude for mid-infrared antennas for which typically $\lambda/a \simeq 5$ and $h/a \simeq 10$. Our first concern will thus be to validate our results by comparing them with the results of well established simulation tools. For this purpose, we use here FDTD simulations realized with a commercial software (Lumerical FDTD) as a reference. (3) We consider the antenna to be surrounded by a uniform medium with an effective index $n_{\text{eff}} = 2.6$. This value is such that the scattering resonance curve for a straight rod antenna embedded in a uniform dielectric of index n_{eff} overlaps with the scattering resonance curve of the same antenna located at an interface between silicon and air, both curves being obtained by FDTD simulations. Although imperfect, our approach offers the advantage to preserve simplicity and comparisons with FDTD simulations will show that it is accurate enough to guide the design of optical components, answering doubts expressed in the past that the numerical solution presented here would accurately handle wire antennas in a space partially filled with dielectric medium[15,16], such as antennas defined on a dielectric substrate. (4) The finite conductivity of gold is taken into account in our calculations (details in the Appendix) and is derived from the optical constants found in [17].

Our solution follows the outline of the derivation presented in [7] for the numerical integration of Pocklington's equation in the case of a straight cylindrical rod antenna. We first derive the integral equation governing the behavior of V-shaped cylindrical antennas, reduce the two-dimensional problem to one dimension, and implement a numerical solution based on the MoM. We first obtain the current distribution driven at the surface of the antenna by a known incident field. The far-field scattered by the antenna in any direction, with amplitude, phase and polarization information, is then calculated as the coherent sum of the fields scattered by a series of infinitesimal current elements distributed along the antenna and having their amplitude and phase given by

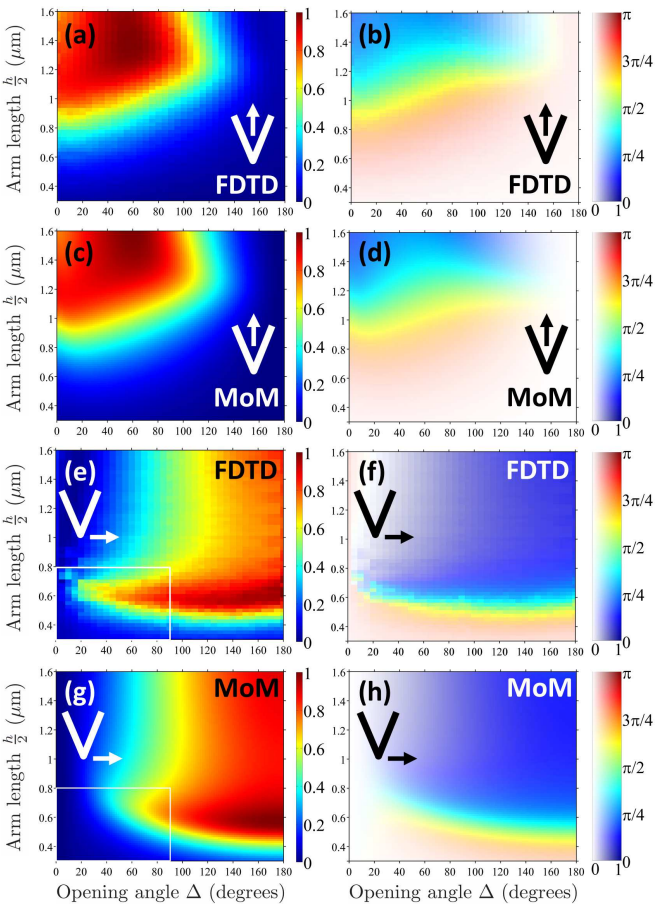

FIG. 2. (a) and (c) (resp. (b) and (d)): Amplitude (resp. Phase) of the scattered field in the direction normal to the plane of the antenna, for an incident electric field oriented parallel to the symmetric mode (see insets and Fig. 1), obtained with FDTD calculations ((a) and (b)) and our MoM numerical solution ((c) and (d)), for different antenna geometries. (e)-(h) are similar to (a)-(d), but for an incident electric field oriented parallel to the anti-symmetric mode. Details of the FDTD simulations are provided in the Appendix. For the phase plots, the colors encode the phase and we superposed a white mask whose transparency is proportional to the amplitude of the scattered field: the lower the amplitude, the whiter the pixel (see color bar). This enables to highlight the significant areas of the plot only, i.e. the one were the scattered amplitude is strong. A white frame is added in (e) and (g) to highlight the region where our approximations are least valid and where the main differences are observed between our MoM calculations and FDTD simulations. The FDTD maps have 57x37 cells, each corresponding to a different three dimensional simulation. The MoM maps have 100x100 cells.

the current distribution, using an analytical expression for the radiation pattern of interfacial dipoles[18]. The numerical solution is detailed in the Appendix.

III. RESULTS

A. Comparison with FDTD

In order to compare our results with FDTD simulations, we calculated the far-field amplitude and phase of the scattered field, for different antenna lengths h, ranging from 0.6 μm (total length) to 3.2 μm, and different opening angles Δ, ranging from 0 to 180°. The antenna is illuminated by a plane wave coming at normal incidence with respect to the antenna plane. The details of the FDTD simulations are provided in the Appendix. In Fig. 2, we present the calculated amplitude and phase response of the V-shaped antennas, in the direction normal to the antenna plane, for an incident electric field oriented either along the symmetric ((a)-(d)) or anti-symmetric ((e)-(h)) plasmonic mode (see inset schematics).

We observe a very good agreement between FDTD calculations and our MoM calculations, demonstrating that our calculations give an accurate picture of the phase and amplitude response of nanoscale V-shaped antennas. Importantly, each point on the map is calculated in about 10 ms on a desktop computer using our method, compared to about 15 minutes for the corresponding FDTD simulation. In order to obtain the full map with 57x37 points, each corresponding to a different geometry and thus requiring a new three dimensional simulation, three weeks of computation is needed for FDTD, while only about 100 seconds is required with our method to obtain 100x100 points.

In the symmetric mode (Fig. 2 (a)-(d)), excited by an incident electric field parallel to the axis of symmetry of the antenna, the current distribution in each arm approximates that of an individual straight antenna of length $h/2$ and therefore the first-order antenna resonance occurs at $h/2 \simeq \lambda_0/(2.n_{\text{eff}})$[19]. In the antisymmetric mode (Fig. 2 (e)-(h)), excited by an incident electric field perpendicular to the axis of symmetry of the antenna, the current distribution in each arm approximates that of one half of a straight antenna of total length h and the condition for the first-order resonance of this mode is $h \simeq \lambda_0/(2.n_{\text{eff}})$. These features can be observed in Fig. 2, where a maximum of the scattered field amplitude is observed when a resonance condition is satisfied. We also observe a phase shift of magnitude approximately equal to π across the resonances, as is expected across any resonance.

The scattered field amplitude vanishes for large (resp. small) opening angles Δ for a symmetric (resp. antisymmetric) excitation, corresponding to the evolution of the scattering cross-sections with opening angle. We note that for the symmetric mode, the results from our numerical solution are still in very good agreement with FDTD for small Δ, where near-field interactions between the two arms are expected to be maximum. This suggests that distortions of the current distributions induced by coupling effect between the two arms are well accounted for in our numerical solution.

The scattering amplitude at small opening angles ($\Delta < 90°$) and close to the first anti-symmetric resonance (Fig. 2 (e) and (g), within the white frame), shows the main divergence between our calculations and FDTD simulations. This region (the lower left corner) corresponds to the region where the thin-wire approximation is the least valid since the arm length is only two to three times larger than the antenna diameter. We observe that the scattering amplitude decays faster in our MoM calculations than in FDTD simulations as the opening angle is reduced. The geometry simulated by FDTD (see Fig. 1 (b)) is such that there is always a significant portion of the antenna, in particular at the junction, that is oriented parallel to the anti-symmetric excitation (i.e. perpendicularly to the antenna symmetry axis). This is a result of the finite width of the arms. We thus expect a slow decrease of the scattering cross-section with decreasing opening angle. In contrast, the effective geometry considered in our MoM calculations is that of an infinitely thin wire. This effect is thus not taken into account and we expect the scattering cross-section to decrease faster with decreasing opening angles. In the rest of this work, we will leave out this region in our discussion of the results.

One could expect in a first order approximation that as the opening angle is reduced for a fixed antenna length, the resonance position does not move and only the scattering cross section is reduced. However, the 'tilted' shape of the symmetric resonance in Fig. 2 (a) and (c) suggests the opposite. The red-shift (resp. blue-shift) of the resonance as the opening angle is reduced for the symmetric (resp. anti-symmetric) mode is a result of the interaction between the two arms of the V-shaped antennas. Charges of similar (resp. opposite) signs accumulating at both extremities of the antenna contribute to a weaker (resp. stronger) restoring force in the symmetric (resp. anti-symmetric) mode, and thus a red-shift (resp. blue-shift). We note that we use the expressions red- and blue-shift even though our results are for a fixed wavelength because we translate a resonance shifting to a longer (resp. shorter) antenna length as a blue-shift (resp. red-shift) of the resonance.

The polarization of the scattered radiation is the same as that of the incident light when the latter is polarized parallel or perpendicular to the antenna symmetry axis. However, for an arbitrary incident polarization, both antenna modes are excited with different amplitude and phase because of their distinct resonance conditions. As a result, the scattered light can have a different polarization from that of the incident light. In Fig. 3 (a) and (b), we show the amplitude and phase of the scattered field component polarized perpendicularly to the incident polarization, which is itself polarized at 45° with respect to the symmetry axis of the antenna. the plots are obtained with our MoM numerical solution. The two areas of highest amplitude correspond to the resonant excitation of either the symmetric or the antisymmetric mode. Across each of these resonances, a π phase shift is observed, so that overall a coverage of almost the full 2π range can be achieved[1].

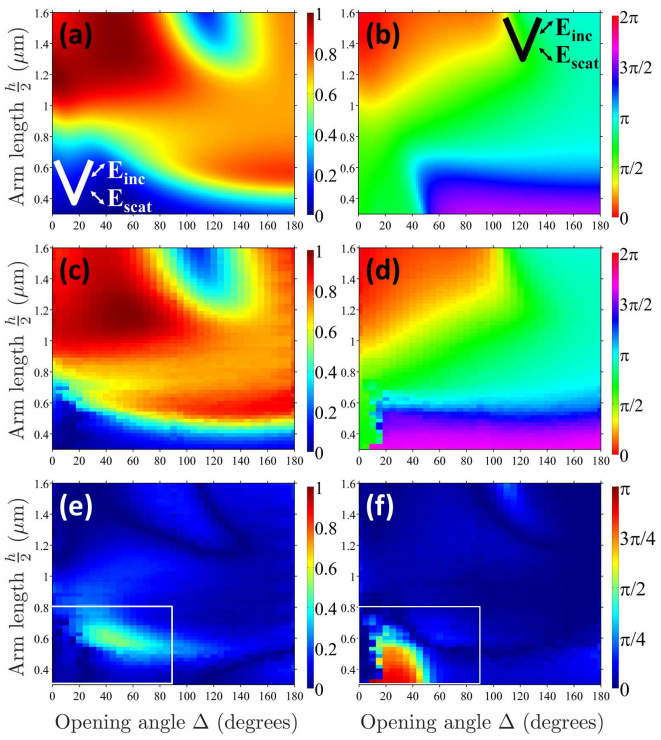

FIG. 3. Amplitude ((a) and (c)) and Phase ((b) and (d)) of the scattered field component polarized perpendicularly to the incident polarization for different antenna geometries. The incident electric field is polarized at 45° with respect to the symmetry axis of the antenna. (a) and (b) are obtained with our MoM numerical solution while (c) and (d) are obtained with FDTD simulations. Details of the FDTD simulations are provided in the Appendix. (e) and (f) correspond respectively to the absolute difference between (a) and (c) (amplitude) and (b) and (d) (phase). A white frame is added in (e) and (f) to highlight the region where the main differences are observed between our MoM calculations and FDTD simulations.

In Fig. 3 (c) and (d), we show for comparison purposes the same quantities as in Fig. 3 (a) and (b), as obtained with FDTD simulations. The absolute differences between the results of the two calculation methods are shown in Fig. 3 (e) and (f), respectively for the amplitude and the phase of the cross-polarized scattered field. Except for the lower left corner already discussed above, the two methods are in agreement to within ≈ 0.15 in amplitude, and $\pi/10$ in phase. These results demonstrate that resonant mid-infrared plasmonic antennas are within the domain of validity of our approximations. The errors observed (lower left corner) stem from distortions of the antenna response created by the finite width of the antenna. Provided the antenna geometry has a sufficient aspect ratio between the width and the length of the antenna, on the order of 1:4, such errors remain small.

Using the maps presented in Fig. 3 (a) and (b), one

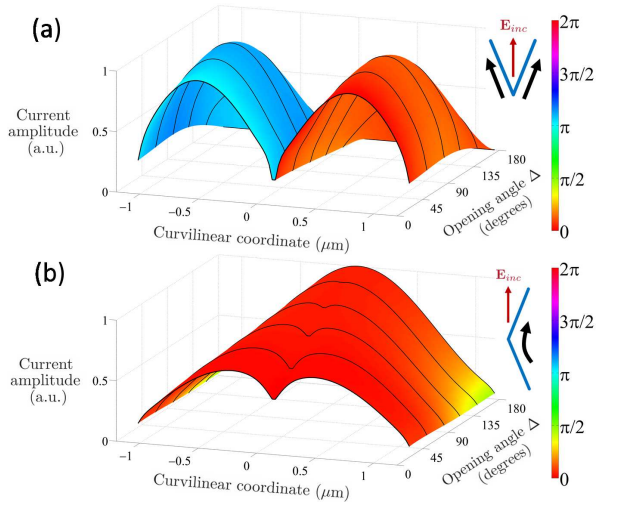

FIG. 4. (a) Current distribution along an antenna of total length $h = 2.4$ μm for opening angles Δ from 30 to 180°. The incident electric field is polarized along the symmetric mode (see inset). The incident wavelength is $\lambda_0 = 7.7$ μm. The height indicates the amplitude of the current while the phase is given by the color. (b) is similar to (a), for an incident electric field polarized along the anti-symmetric mode (see inset). The black line are drawn at regular intervals of 30° in order to outline the amplitude variations of the current distribution. The position along the antenna is indicated by the curvilinear coordinate running along the antenna from one end to another, with its origin at the junction. Black arrows on the inset schematics of the antennas indicate the direction of the current in each arm for the symmetric and anti-symmetric modes.

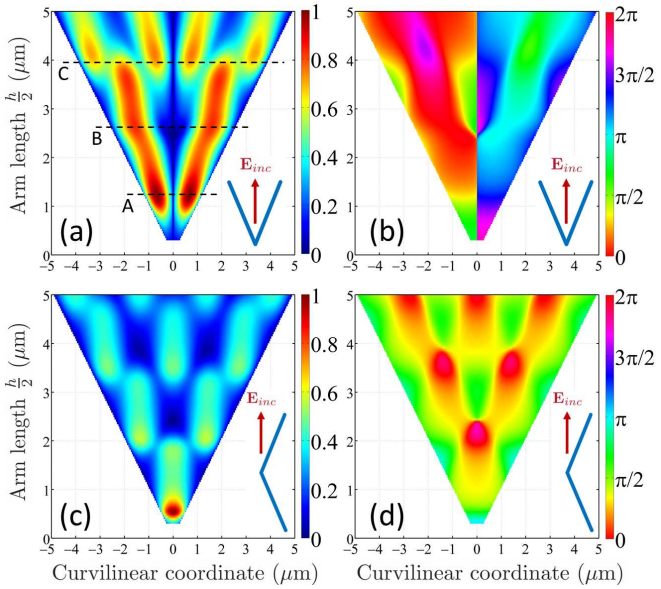

FIG. 5. (a) Amplitude and (b) Phase of the current along an antenna with opening angle $\Delta = 45°$ and total antenna length varying from to 0.6 to 10 μm. The incident electric field is polarized along the symmetric mode. The incident wavelength is $\lambda_0 = 7.7$ μm. The labels A, B and C indicate the position of the first three resonances observed. (c) and (d) are similar to (a) and (b) for an incident electric field polarized along the anti-symmetric mode and for an opening angle $\Delta = 135°$.

can quickly explore a large design-parameter space for V-shaped antennas, choose antennas with specific amplitude and phase response in the cross polarization, and assemble them to form an arbitrary phase and amplitude profile. For examples, for the phase-gradient plate used in [1], antennas with similar scattering amplitudes and regularly spaced scattering phases were chosen.

B. Current distribution

As mentioned above, we approximate the current to be purely axial. The current distribution is then fully described once given the complex value of the current as a function of the curvilinear coordinate running along the antenna length, as plotted in Fig. 4 for a constant antenna length $h = 2.4$ μm and for opening angles Δ varying from 30° to 180°. The π phase difference between the two arms for the symmetric mode (Fig. 4 (a)) indicates that the current flows in opposite direction in the two arms. We note here that we define the direction of the current with respect to the curvilinear coordinate orientation running from one end of the antenna to the other. There is a node of current at the center of the antenna. This agrees well with the picture of the symmetric mode being analogous to the mode supported by two parallel individual straight antennas of length $h/2$. In contrast, the asymmetric mode (Fig. 4 (b)) features a single lobe consistent with it being approximately equivalent to the mode of a single straight antenna of total length h.

The small distance between the two arms leads to near-field coupling translating into distortions of the current near the junction, especially for small opening angles. This is illustrated by the central dip which appears in the current distribution of the anti-symmetric mode for small opening angles. This feature can be easily understood since, for $\Delta < 90°$, the electric field radiated by the current in one arm opposes the current in the other arm. On the contrary, a small increase of the current near the junction can be observed for the symmetric mode (and for $\Delta < 90°$), since now the electric field radiated by one arm contributes to drive the current in the other arm.

Fig. 5 shows the current distribution along the antenna (with the position indicated by the curvilinear coordinate) for opening angles $\Delta = 45°$ ((a) and (b), with the incident electric field polarized along the symmetric mode) and $\Delta = 135°$ ((c) and (d), with the incident electric field polarized along the anti-symmetric mode) and different arm-lengths $h/2$. We can observe the appearance of the higher order modes with increasing length.

For the symmetric mode (Fig. 5 (a)-(b)), the single lobe observed in each arm for $h/2 \simeq \lambda_0/(2.n_{\text{eff}})$ (A) splits into three lobes for $h/2 \simeq 3\lambda_0/(2.n_{\text{eff}})$ (C). This is again consistent with the picture of the symmetric mode being analogous to the mode supported by two parallel individual straight antenna of length $h/2$. Interestingly, we observe an intermediate resonance for $h/2 \simeq 2\lambda_0/(2.n_{\text{eff}})$ (B), whose excitation should be prohibited by symmetry considerations. The coupling between the two arms enables to couple energy into this mode. Other details of the current distribution indicate the effects of near-field coupling between the two arms, such as the asymmetry in the three-peak high-order pattern observed in each arm for $h/2 = 4$ μm (C): the side-lobe closer to the junction does not have the same shape as the one close to the extremity of the antenna. For the anti-symmetric mode (Fig. 5 (c)-(d)), the single lobe observed at $h \simeq \lambda_0/(2.n_{\text{eff}})$ splits into three (and then five, seven,...) lobes for h equal to odd integer multiples of $\lambda_0/(2.n_{\text{eff}})$, in agreement with it being approximately equivalent to the mode of a single straight antenna of total length h.

C. Far-field radiation pattern

We now study the far-field radiation pattern of a given V-shaped antenna with $\Delta = 135°$ and $h/2 = 1.2$ μm. The geometry and the definition of the far-field coordinates are represented in Fig. 6 (a) and the current distribution is shown in Fig. 6 (b). The angle α between the symmetry axis of the antenna and the incident polarization is 45°. The current distribution is a superposition of a symmetric and an anti-symmetric mode, featuring two lobes reminiscent of the first order symmetric mode and a non-vanishing current at the junction as for the anti-symmetric modes.

In Fig. 6 (c), we show the amplitude of the cross-polarized scattered field. The far-field is calculated as the coherent sum of the far-fields radiated by infinitesimal current elements distributed along the antenna, having phase and amplitude following the current distribution plotted in Fig. 6 (b). The cross-polarized scattered field, i.e. the scattered field component resulting from a 90°-polarization conversion process, is obtained as the coherent sum of the fields radiated by the projections of these current elements on the x-axis. The information on the position of the current elements one relative to the other along the antenna is kept in order to calculate the interference of the fields radiated by different current elements. Note that the phase difference between the fields radiated by different current elements contains a geometric term as well as a term coming from the non-uniform phase of the current distribution along the antenna. We observe that the main lobe is not in the direction normal to the plane of the antenna, as a result of interference between the fields radiated by different sections of the antenna. The symmetry of the antenna is not preserved

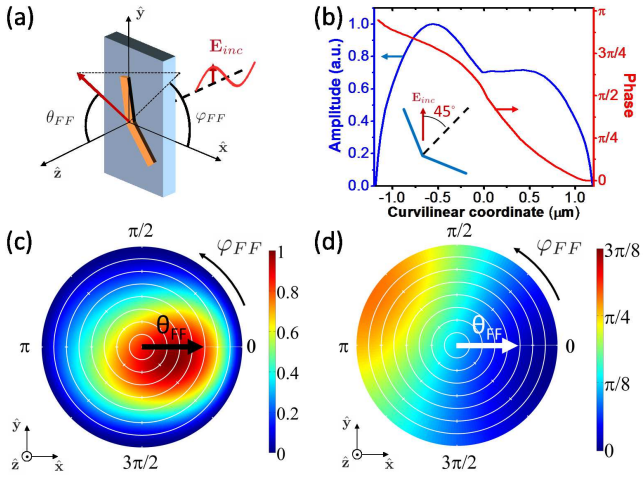

FIG. 6. (a) Schematic with definition of the far-field coordinates (θ_{FF}, φ_{FF}). The incident electric field is propagating along the z-axis and is polarized along the y-axis. The antenna is in the x-y plane. (b) Current distribution (amplitude and phase) for a V-shaped antenna with $\Delta = 135°$ and $h/2 = 1.2$ μm. The angle α between the symmetry axis of the antenna and the incident polarization is 45° (see inset schematic), in order to excite both symmetric and anti-symmetric modes. (c) Corresponding amplitude and (d) phase of the cross-polarized scattered field for different far-field coordinates (θ_{FF}, φ_{FF}). The distance to the center of the plot is proportional to θ_{FF}, with $\theta_{\text{FF}} = 0$ at the center and $\theta_{\text{FF}} = \pi/2$ at the edge. The white circles represent values of θ_{FF} regularly spaced from 0 to $\pi/2$. The azimuthal angle of the plot is equal to φ_{FF}.

in the far-field since the incident electric field is not along one of the antenna symmetry or antisymmetry axis. The asymmetric amplitude and phase profile of the current distribution in Fig. 6 (b) also illustrates this point. The scattered intensity vanishes in all directions parallel to the antenna plane. This is a known result for dipoles located at an interface between two different dielectric media[18].

The phase of the cross-polarized scattered field is shown in Fig. 6 (d). It is interesting to observe that it is not constant, with variations on the order of $\pi/8$ over the main scattering lobe. A good knowledge of the amplitude and phase profile of the scattered field over the full half space is important to optimize optical components relying on the precise engineering of the scattering of the antennas at large angles, such as short focal-distance flat lenses.

IV. CONCLUSION

In summary, using the Integral Equation Method of Moments, we presented an accurate and efficient numerical computation of the current distribution in V-shaped

antennas excited by an electric field of arbitrary polarization. Using this information, we extracted the far-field phase, amplitude and polarization response of these elements in any direction. We demonstrated the accuracy of our numerical solution by comparing the results with FDTD simulations. The key element leading to the increased computational efficiency is the use of the thin-wire approximation which effectively reduces the problem to one dimension. This approximation necessitates aspect ratios of at least 1:4 between the width and the length of the antenna. We discussed details of the current distribution related to near-field coupling between the two arms of the antennas. The numerical method presented here enables a fast probing of the large design-parameter space of V-shaped antennas, that have been shown to be essential building blocks for optical elements relying on phase discontinuities[1].

ACKNOWLEDGMENTS

The authors acknowledge helpful discussion with A. Kabiri, and support from the National Science Foundation (NSF), Harvard Nanoscale Science and Engineering Center (NSEC) under contract NSF/PHY 06-46094. This work was supported in part by the Defense Advanced Research Projects Agency (DARPA) N/MEMS S&T Fundamentals program under grant N66001-10-1-4008 issued by the Space and Naval Warfare Systems Center Pacific (SPAWAR). M.A.K. is supported by NSF through a Graduate Research Fellowship. Z.G. acknowledges funding from the European Community's Seventh Framework Programme (FP7/2007-2013) under grant agreement PIOF-GA-2009-235860.

APPENDIX

1. *General problem*

Our solution is inspired by the derivation found in [7] of the numerical integration of Pocklington's equation in the case of a straight rod antenna. After deriving the integral equation governing the behavior of V-shaped antennas, we generalize the numerical solution to a two-dimensional problem.

We initially want to solve for the current distribution driven at the surface of the antenna by a known incident field $\mathbf{E_{inc}}$. By either assuming that the antenna is made of perfect electric conductor (PEC), or by modeling accurately the finite conductivity of a real metal, we obtain a relation between the incident and the scattered electric field $\mathbf{E_{scat}}$, valid at the surface of the antenna. Using Maxwell's equations for the scattered field we further link the scattered field at the surface of the antenna and the current that radiates it. We thus finally obtain an integral equation expressing the scattered field as a function of the current distribution. Using a numerical method, we can then invert this equation and solve for the current. Once the current distribution is known, we are able to derive the electric field $\mathbf{E_{scat}}$ scattered by the antenna in all space (we initially only knew $\mathbf{E_{scat}}$ at the surface of the antenna) and thus infer the far-field response in amplitude, phase and polarization, in any direction. Fig. 7 (a) describes the geometry and defines the parameters used in the following derivation.

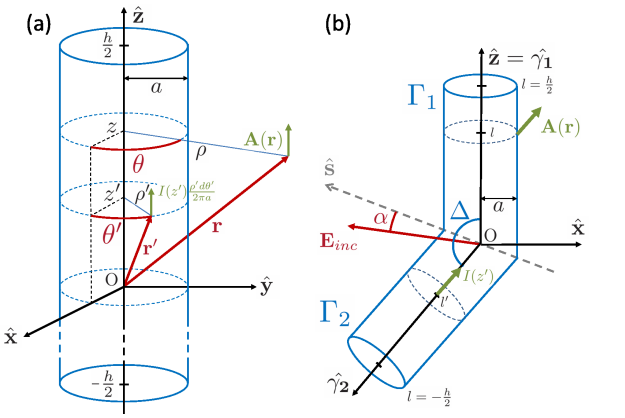

FIG. 7. (a) Schematic of a cylindrical antenna of radius a and total length h. We represented the vector potential $\mathbf{A}(\mathbf{r})$ at point $\mathbf{r}(\rho, \theta, z)$, radiated by the element of current $I(z')\frac{\rho' d\theta'}{2\pi a}$ at point $\mathbf{r}'(\rho', \theta', z')$. (b) Schematic of a V-shaped antenna with opening angle Δ. Note that the vector potential radiated by an element of current in one arm is not parallel to the other arm. The orientation of the antenna with respect to the incident electric field is defined by the angle α between the axis of symmetry of the antenna and the electric field polarization.

We start from Maxwell's equations to connect the scattered fields $\mathbf{E_{scat}}$ and $\mathbf{B_{scat}}$ to the current and charge sources[20]:

$$\nabla \cdot \mathbf{B_{scat}} = 0, \tag{1a}$$
$$\nabla \times \mathbf{E_{scat}} = -j\omega \mathbf{B_{scat}}, \tag{1b}$$
$$\nabla \cdot \mathbf{E_{scat}} = \frac{\rho}{\epsilon_0 \epsilon_r}, \tag{1c}$$
$$\nabla \times \mathbf{B_{scat}} = \mu_0 \mathbf{J} + \frac{j\omega n^2}{c^2} \mathbf{E_{scat}} \tag{1d}$$

We assume here that the antenna is embedded in a uniform dielectric medium with refractive index $n = \sqrt{\epsilon_r}$.

From Eqs. (1a) and (1b), we infer the existence of the magnetic and electric potentials $\mathbf{A}$ and φ satisfying:

$$\mathbf{E_{scat}} = -\nabla\varphi - j\omega\mathbf{A}, \tag{2a}$$
$$\mathbf{B_{scat}} = \nabla \times \mathbf{A} \tag{2b}$$

Substituting Eq. (2) and the Lorenz gauge $\nabla \cdot \mathbf{A} + j\omega\mu_0\epsilon_0\epsilon_r\varphi = 0$ into Eqs. (1c) and (1d), we obtain the

Helmholtz wave equation for the potentials:

$$\nabla^2\varphi + k^2\varphi = -\frac{\rho}{\epsilon_0\epsilon_\mathrm{r}} \tag{3a}$$

$$\nabla^2\mathbf{A} + k^2\mathbf{A} = -\mu_0\mathbf{J} \tag{3b}$$

where $k = \omega n/c$.

In order to find a solution to Eq. (3b), we introduce the Green function $G(\mathbf{r})$, solution of the Green problem $\nabla^2 G(\mathbf{r}) + k^2 G(\mathbf{r}) = -\delta(\mathbf{r})$, where δ is the Dirac delta distribution. In a three-dimensional space, the solution is given by $G(\mathbf{r}) = \frac{e^{-jk|\mathbf{r}|}}{4\pi|\mathbf{r}|}$. We then write the solution of Eq. (3b) as the convolution of $G(\mathbf{r})$ with the current source $\mu_0 J$:

$$\mathbf{A}(\mathbf{r}) = (G * \mu_0\mathbf{J})(\mathbf{r}) = \frac{\mu_0}{4\pi}\iiint_{\mathbb{R}^3}\mathbf{J}(\mathbf{r}')\frac{e^{-jk|\mathbf{r}-\mathbf{r}'|}}{|\mathbf{r}-\mathbf{r}'|}d\mathbf{r}' \tag{4}$$

For a rod made of a perfect electric conductor with vanishing skin depth, conservation of the tangential component of the electric field at the rod surface gives:

$$\hat{\mathbf{z}}\cdot(\mathbf{E_{scat}}(\rho=a) + \mathbf{E_{inc}}(\rho=a)) = 0, \tag{5}$$

where $\hat{\mathbf{z}}$ is a unit vector tangential to the antenna at the point where Eq. (5) is evaluated. In the case of a straight antenna, $\hat{\mathbf{z}}$ is parallel to the antenna axis. We study later how this relation is modified in the case of a real metal with finite conductivity. We consider the current to be limited to the surface of the rod ($\rho = a$). This is exact in the case of a perfect electric conductor and represents an approximation in the case of real metals. Furthermore, using the thin-wire approximation ($a << \lambda$ and $a << h$), we can consider the current distribution $\mathbf{J}(\mathbf{r})$ to be axial and azimuthally invariant[16]. We can thus define the quantity $I(z)$ such that $\mathbf{J}(\mathbf{r}) = \hat{\mathbf{z}}I(z)\delta(\rho-a)\frac{1}{2\pi a}$. A sharp angle on the antenna, as in the case of the V-antennas discussed later, could break down this approximation. However, since a current element at one point affects the vector potential at another point with a magnitude decaying as the inverse of the distance between the two points (see Eq. 4), the perturbation introduced by a sharp angle will remain local so that we can still consider the approximation valid along the entire antenna, except in the immediate vicinity of the junction.

We can now rewrite Eq. (4) as:

$$\begin{aligned}\mathbf{A}(\mathbf{r}) &= \frac{\mu_0}{4\pi}\iiint_{\mathbb{R}^3}\hat{\mathbf{z}}'I(z')\delta(\rho'-a)\frac{e^{-jk|\mathbf{r}-\mathbf{r}'|}}{2\pi a|\mathbf{r}-\mathbf{r}'|}\rho' d\rho' d\phi' dz' \\ &= \frac{\mu_0}{4\pi}\int_{-\frac{h}{2}}^{\frac{h}{2}}\hat{\mathbf{z}}'I(z')dz'K(|\mathbf{r}-\mathbf{r}'|),\end{aligned} \tag{6}$$

where we introduced the kernel $K(|\mathbf{r}-\mathbf{r}'|)$ as:

$$K(|\mathbf{r}-\mathbf{r}'|) \equiv \frac{1}{2\pi}\int_0^{2\pi}\frac{e^{-jk|\mathbf{r}-\mathbf{r}'|}}{|\mathbf{r}-\mathbf{r}'|}d\phi', \tag{7}$$

Additionally, substituting the Lorenz gauge in Eq. (2a), we obtain:

$$\mathbf{E_{scat}} = \frac{1}{j\omega\mu_0\epsilon_0\epsilon_\mathrm{r}}[\nabla(\nabla\cdot\mathbf{A}) + k^2\mathbf{A}] \tag{8}$$

Writing this equation at the surface of the antenna, where we can express $\mathbf{E_{scat}}$ as a function of the known incident field $\mathbf{E_{inc}}$, we can solve Eqs. (6) and (8) for the current distribution I(z). Once the source current is known, we can determine $\mathbf{E_{scat}}$ in any point of space. Because we approximate the current as flowing only along a wire, we are only solving for a scalar quantity. Thus, solving a scalar equation is enough and we will use the projection of Eq. (8) on the tangent to the antenna at each point to obtain J.

Combining Eqs. (5), (6) and (8) leads to a Pocklington-type equation[11]. This equation has no exact analytical solution. However, it can be studied numerically. In order for the numerical solution to be tractable in a reasonable time, we use an approximation for the expression of the kernel defined in Eq. (7). Using again the thin-wire approximation, we can simplify the kernel by observing that the distance $|\mathbf{r}-\mathbf{r}'|$ is basically independent of ϕ' and, in the case of a straight antenna, approximately equal to $R_r = \sqrt{(z-z')^2 + a^2}$. We will refer to this simplified expression as the *effective* distance. We thus obtain the *reduced* kernel $K_r(z-z') = \frac{e^{-jkR_r}}{R_r}$. This approximation is valid as long as $|\frac{z-z'}{a}|$ is not too close to zero. Indeed, we notice that $K_r(0) = \frac{e^{-jka}}{a}$ whereas the exact kernal K diverges for $|\mathbf{r}-\mathbf{r}'| \to 0$. We will come back to this issue when explaining the details of our numerical solution.

2. *V-shaped antennas*

We now consider the case of a V-shaped antenna as represented is Fig. 7 (b). The two arms of the antenna are Γ_1 and Γ_2, respectively in the directions $\hat{\gamma_1}$ and $\hat{\gamma_2}$. For convenience, we choose $\hat{\gamma_1}$ to be collinear to the $\hat{\mathbf{z}}$ axis. The angle between the two arms, oriented in the positive direction from $\hat{\gamma_1}$ to $\hat{\gamma_2}$, is Δ. We consider the curvilinear coordinate l along the antenna length, with origin at the junction point O, positive on Γ_1 and negative on Γ_2. For the sake of simplicity, we consider that the two arms have equal length $h/2$. However, the solution could be easily generalized to an asymmetric configuration with two different arm-lengths.

The effective distance between a current source at coordinate l' and the observation point (x,z) for the vector potential can be written as $R_r(x,z,l',\Psi) = \sqrt{a^2 + (z + l'\cos(\Psi))^2 + (x - l'\sin(\Psi))^2}$, where $\Psi = \pi$ if l and l' are on the same arm, and $\Psi = \Delta$ otherwise. We note that the expression for a linear antenna is recovered by setting $\Psi = \pi$, $l' = z'$ and $x = 0$. The term a^2 comes from the thin-wire approximation. Using this effective distance, we can define a reduced kernel as introduced above: $K_r(x,z,l') = \frac{e^{-jkR_r}}{R_r}$. We consider here that the observation point is in the z-x plane of the antenna. This is justified by the thin-wire approximation for which azimuthal variation of the current on the wire surface is neglected. In other terms, we consider that the

current is only a function of the curvilinear coordinate l.

Now that the problem is two dimensional, the vector potential radiated by an element of current at one point of the antenna is not always parallel to the antenna at another point. This represents the main challenge of the calculation presented here. In writing Eq. (8), cross derivatives now appear for the term $\nabla(\nabla\cdot\mathbf{A})$:

$$\nabla(\nabla\cdot\mathbf{A})\cdot\hat{\mathbf{z}} = \left[\frac{\partial}{\partial z}(\frac{\partial}{\partial z}A_z + \frac{\partial}{\partial x}A_x)\right] \tag{9}$$

We can directly compute the expression $\frac{\partial}{\partial x}A_x$ from the analytical expression of A_x, written using the reduced kernel introduced above:

$$A_x(x,z) = \frac{\mu_0}{4\pi}\int_{-\frac{h}{2}}^{0} I(l')\frac{e^{-jkR_r(x,z,l',\Delta)}}{R_r(x,z,l',\Delta)}dl'(-\hat{\gamma_2}.\hat{\mathbf{x}}) \tag{10}$$

Note that only the current flowing in Γ_2 creates a non-vanishing component of $\mathbf{A}$ along the x-axis, hence the integration is limited to $[-h/2, 0]$. We then obtain:

$$\frac{\partial}{\partial x}A_x\big|_{x=0}(x,z) = \frac{\mu_0}{4\pi}\int_{-\frac{h}{2}}^{0} I(l')\frac{e^{-jkR_r}}{R_r^3}(1+jkR_r)\sin^2(\Delta)l'dl' \tag{11}$$

We now write Eq. (8), evaluated in $x=0$ and $z=l$, for all $l\in\Gamma_1$, using (6) and (11), and we obtain a Pocklington-type equation generalized to our two dimensional problem:

$$\left[\frac{\partial^2}{\partial l^2}+k^2\right]\left(\frac{j\eta}{2\pi}\int_{-\frac{h}{2}}^{\frac{h}{2}} I(l')\tilde{K_1}(l,l',\Delta)dl'\right) + \left[\frac{\partial}{\partial l}\right]\left(\frac{j\eta}{2\pi}\int_{-\frac{h}{2}}^{\frac{h}{2}} I(l')\tilde{K_2}(l,l',\Delta)dl'\right) = 2kE_{\gamma_1}(l), \quad \forall l\in\Gamma_1 \tag{12}$$

where:

$$\tilde{K_1}(l,l',\Delta) = -\frac{e^{-jkR_r(0,l,l',\Delta)}}{R_r(0,l,l',\Delta)}H(-l')\cos(\Delta) + \frac{e^{-jkR_r(0,l,l',\pi)}}{R_r(0,l,l',\pi)}H(l'),$$

$$\tilde{K_2}(l,l',\Delta) = \sin^2(\Delta)\frac{e^{-jkR_r(0,l,l',\Delta)}}{R_r^3(0,l,l',\Delta)}\left(1+jkR_r(0,l,l',\Delta)\right)l'H(-l')$$

The Heaviside function H (defined as $H(l)=1, \forall l\geq 0$ and $H(l)=0, \forall l<0$) was used to distinguish contributions to the vector potential $\mathbf{A}$ from Γ_1 ($l'>0$) and Γ_2 ($l'<0$), respectively. We introduced two reduced kernels $\tilde{K_1}$ and $\tilde{K_2}$ containing, respectively, the terms A_z (from both arms) and $\frac{\partial}{\partial x}A_x$ (only from Γ_2). The projection of the incident field $\mathbf{E_{inc}}$ on $\hat{\gamma_1}$ is used: $E_{\gamma_1}(l) = \mathrm{E_{inc}}\cos\left(\frac{\Delta}{2}+\alpha\right)$, where α defines the incident polarization (see Fig. 1 (c)). The constant $\eta = \sqrt{\frac{\mu_0}{\epsilon_0\epsilon_r}}$ is introduced.

Eq. (12) is valid for all points along Γ_1, i.e. it links the current distribution over the whole antenna and the vector potential on the surface of Γ_1. We now obtain the second half of the equation ($l\in\Gamma_2$) by symmetry considerations ($\Delta\to-\Delta$, $I\to-I$, $l\to-l$ and $l'\to-l'$) and introducing the projection of the incident field on $\hat{\gamma_2}$, $E_{\gamma_2}(l) = \mathrm{E_{inc}}\cos\left(\frac{\Delta}{2}-\alpha\right)$:

$$\left[\frac{\partial^2}{\partial l^2}+k^2\right]\left(\frac{j\eta}{2\pi}\int_{-\frac{h}{2}}^{\frac{h}{2}} I(l')\tilde{K_1}(-l,l',\Delta)dl'\right) - \left[\frac{\partial}{\partial l}\right]\left(\frac{j\eta}{2\pi}\int_{-\frac{h}{2}}^{\frac{h}{2}} I(l')\tilde{K_2}(-l,l',\Delta)dl'\right) = -2kE_{\gamma_2}(l), \quad \forall l\in\Gamma_2 \tag{13}$$

We used here the symmetry of our particular geometry to simplify the derivation. When treating asymmetric geometries, one has to rederive the equation governing the second arm, but the general idea of the derivation remains the same.

We can now gather Eqs. (12) and (13) into a single equation valid for all l in $\Gamma_1\cup\Gamma_2$:

$$\left[\frac{\partial^2}{\partial l^2}+k^2\right]V^{(1)}(l) + \left[\frac{\partial}{\partial l}\right]V^{(2)}(l) = 2kE(l), \quad \forall l\in\Gamma_1\cup\Gamma 2, \tag{14}$$

where $E(l) = E_{\gamma_1}(l)H(l) + E_{\gamma_2}(l)H(-l)$. We introduced:

$$V^{(1)}(l) \equiv \frac{j\eta}{2\pi}\int_{-\frac{h}{2}}^{\frac{h}{2}} I(l')\big[\tilde{K_1}(l,l',\Delta)H(l) - \tilde{K_1}(-l,l',\Delta)H(-l)\big]dl' \tag{15}$$

and

$$V^{(2)}(l) \equiv \frac{j\eta}{2\pi}\int_{-\frac{h}{2}}^{\frac{h}{2}} I(l')\big[\tilde{K_2}(l,l',\Delta)H(l) + \tilde{K_2}(-l,l',\Delta)H(-l)\big]dl' \tag{16}$$

3. Numerical solution

As mentioned above, Pocklington's integral equation cannot be solved analytically. Here we extend the numerical solution presented in [7] to a two-dimensional problem.

The curvilinear coordinate $l\in[-\frac{h}{2},\frac{h}{2}]$ is discretized into a vector $\mathcal{L} = [l_{-M}, l_{-M+1}, ..., l_M]$ with $N = 2M+1$ points spaced by a constant step D. We also define $\tilde{V}_n^{(i)} = V^{(i)}(l_n), i=1,2$ and $\tilde{E}_n = E(l_n)$.

The current $I(l)$ is expanded into a sum of basis functions B_n chosen here to be Dirac functions ($B_n(l) = \delta(l - l_n)$):

$$I(l) = \sum_{j=-M}^{M} \tilde{I}_j B_j(l) \tag{17}$$

We note that other basis functions could be chosen, such as triangular or sinusoidal functions. Choosing a basis of Dirac functions greatly simplifies the evaluation of the integral over l' in Eqs. (15) and (16). We obtain:

$$\tilde{V}_n^{(i)} = \sum_{j=-M}^{M} \kappa_{nj}^{(i)} \tilde{I}_j, \text{ or } \tilde{V}^{(i)} = \kappa^{(i)} \tilde{I}, \quad i = 1, 2 \tag{18}$$

where $\kappa^{(i)}$ are the reduced kernel matrices:

$$\kappa_{nj}^{(1)} = \frac{j\eta}{2\pi} \left[\tilde{K_1}(l_n, l_j, \Delta) H(l_n) - \tilde{K_1}(-l_n, l_j, \Delta) H(-l_n) \right]$$
$$\kappa_{nj}^{(2)} = \frac{j\eta}{2\pi} \left[\tilde{K_2}(l_n, l_j, \Delta) H(l_n) + \tilde{K_2}(-l_n, l_j, \Delta) H(-l_n) \right]$$

The thin-wire approximation used when introducing the reduced kernel is valid only as long as the distance between the integration point (l_j) and the observation point (l_n) is large enough compared to the radius a of the antenna. It is thus never valid for the diagonal terms for which $l_j = l_n$. While the exact kernel K diverges for $|\mathbf{r} - \mathbf{r}'| \to 0$, the reduced kernel K_r keeps a finite value. In order to reduce computation time, we set the value of the diagonal terms to $2K_r(0)$, so that the value of the diagonal term is about twice the value of the neighboring non-diagonal terms. This reproduces well the sharp divergence of the exact kernel. Although rather coarse, this approximation gives accurate results, as was confirmed earlier by comparison to FDTD simulations. More refined strategies have been developed to remove the singularity from the kernel in Pocklington's equation and may be of interest for the reader[21,22]. With our approximation, the diagonal terms of the reduced kernel matrices become:

$$\kappa_{nn}^{(1)} = \frac{j\eta}{\pi} \left[\tilde{K_1}(l_n, l_n, \Delta) H(l_n) - \tilde{K_1}(-l_n, l_n, \Delta) H(-l_n) \right]$$
$$\kappa_{nn}^{(2)} = \frac{j\eta}{\pi} \left[\tilde{K_2}(l_n, l_n, \Delta) H(l_n) + \tilde{K_2}(-l_n, l_n, \Delta) H(-l_n) \right]$$

For all non-diagonal terms in the matrices $\kappa^{(i)}$ we empirically determined that we can safely use the reduced kernel expression, provided $\frac{D}{a} \geq 0.2$. As D is further reduced, we observed that the solution becomes unstable since the 'discontinuity' we introduced by setting the value of the diagonal terms becomes sharper than the actual divergence of the exact kernel. A finer computation of the kernel for the terms neighboring the diagonal could be used for increased accuracy. However, our main purpose here is to develop a simple and fast modeling tool to probe a large parameter space so we used the approximate evaluation. In our numerical solution, the total length of the antenna is discretized in 90 points, so that the minimum step size D for the smallest antenna calculated is such that $D/a > 0.2$.

The first and second order derivatives in Eq. (14) are approximated by the following finite difference schemes (neglecting round-off error):

$$\frac{\partial^2}{\partial l^2} V^{(1)}(l)\big|_{l=l_n} = \frac{\tilde{V}_{n+1}^{(1)} - 2\tilde{V}_n^{(1)} + \tilde{V}_{n-1}^{(1)}}{D^2} + \mathcal{O}(D^2)$$
$$\frac{\partial}{\partial l} V^{(2)}(l)\big|_{l=l_n} = \frac{\tilde{V}_{n+1}^{(2)} - \tilde{V}_{n-1}^{(2)}}{2D} + \mathcal{O}(D^2)$$

We can now write the discretized equation corresponding to Eq. (14):

$$\left[\mathcal{A}\kappa^{(1)} + \mathcal{C}\kappa^{(2)} \right] \tilde{I} = \mathcal{Q} d \tilde{E}, \tag{19}$$

where

$$\mathcal{A} = \frac{1}{D^2} \begin{bmatrix} 0 & 0 & 0 & 0 & 0 & \cdots & & & 0 \\ 1 & -2\alpha & 1 & 0 & 0 & \cdots & & & 0 \\ 0 & 1 & -2\alpha & 1 & 0 & \cdots & & & 0 \\ \vdots & & & \ddots & \ddots & \ddots & & & \vdots \\ 0 & & & \cdots & 0 & 1 & -2\alpha & 1 & 0 \\ 0 & & & \cdots & 0 & 0 & 1 & -2\alpha & 1 \\ 0 & & & \cdots & 0 & 0 & 0 & 0 & 0 \end{bmatrix},$$

with $\alpha = 1 - \frac{k^2 D^2}{2}$,

$$\mathcal{C} = \frac{1}{2D} \begin{bmatrix} 0 & 0 & 0 & 0 & 0 & \cdots & & & 0 \\ -1 & 0 & 1 & 0 & 0 & \cdots & & & 0 \\ 0 & -1 & 0 & 1 & 0 & \cdots & & & 0 \\ \vdots & & & \ddots & \ddots & \ddots & & & \vdots \\ 0 & & & \cdots & 0 & -1 & 0 & 1 & 0 \\ 0 & & & \cdots & 0 & 0 & -1 & 0 & 1 \\ 0 & & & \cdots & 0 & 0 & 0 & 0 & 0 \end{bmatrix},$$

and

$$\mathcal{Q} = \begin{bmatrix} 0 & 0 & 0 & 0 & \cdots & & 0 \\ 0 & 1 & 0 & 0 & \cdots & & 0 \\ 0 & 0 & 1 & 0 & \cdots & & 0 \\ \vdots & & & \ddots & & & \vdots \\ 0 & & \cdots & & 0 & 1 & 0 & 0 \\ 0 & & \cdots & & 0 & 0 & 1 & 0 \\ 0 & & \cdots & & 0 & 0 & 0 & 0 \end{bmatrix},$$

and $d = 2k$.

Matrices $\mathcal{A}$, $\mathcal{C}$ and $\mathcal{Q}$ are square N by N matrices. Note that $\mathcal{Q}$ represents the projection on the interior of

the antenna, i.e. excluding the two end-points. We added a first row and a last row of zeros in the matrices $\mathcal{A}$, $\mathcal{C}$ and $\mathcal{Q}$. These rows do not add any equation and ensure that the finite difference schemes are defined for $n = \pm M$. At this point, Eq. (19) represents a system of $N-2$ equations for N unknowns (the N components of the vector $\tilde{I}$). It is therefore not invertible. However, two unknowns are given by the boundary conditions: $I(\frac{h}{2}) = I(-\frac{h}{2}) = 0$, or in matrix form: $(\mathbb{I}_N - \mathcal{Q})\,\tilde{I} = 0$, where $\mathbb{I}_N$ is the N by N identity matrix. We can finally write the discretized Pocklington equation as:

$$\left[\mathcal{A}\kappa^{(1)} + \mathcal{C}\kappa^{(2)}\right]\mathcal{Q}\tilde{I} = \mathcal{Q}d\tilde{E}, \tag{20}$$

Introducing $\bar{\mathcal{Z}} \equiv \left(\left[\mathcal{A}\kappa^{(1)} + \mathcal{C}\kappa^{(2)}\right]\mathcal{Q}\right)_{\substack{2\le n\le N-1,\\ 2\le j\le N-1}}$, $\bar{I} = \tilde{I}_{2\le n\le N-1}$ and $\bar{E} = \tilde{E}_{2\le n\le N-1}$, Eq. (20) takes the form:

$$\left[\begin{array}{c|c|c} 0 & 0 & 0 \\ \hline 0 & \bar{\mathcal{Z}} & 0 \\ \hline 0 & 0 & 0 \end{array}\right]\left[\begin{array}{c} 0 \\ \hline \bar{I} \\ \hline 0 \end{array}\right] = d\left[\begin{array}{c} 0 \\ \hline \bar{E} \\ \hline 0 \end{array}\right]$$

We can thus reduce the system to $N-2$ equations for $N-2$ remaining unknowns (the $N-2$ components of the vector $\bar{I}$), from which we can calculate the discretized current distribution:

$$\bar{I} = d\bar{\mathcal{Z}}^{-1}\bar{E} \tag{21}$$

4. *Modeling real metals*

We have so far assumed that the antenna is made of perfect electric conductor. This assumption was only used in order to derive Eq. 5, i.e. the relation between the incident and the scattered electric field at the surface of the antenna. In the case of real metals, the boundary condition is modified with the introduction of a finite conductivity, and using Ohm's law, we obtain at the surface of the antenna[20]:

$$\mathbf{E}_{\parallel}(\rho = a) =$$
$$\hat{\mathbf{z}} \cdot (\mathbf{E_{scat}}(\rho = a) + \mathbf{E_{inc}}(\rho = a)) = \frac{1-j}{2\pi a}\sqrt{\frac{\mu_0\omega}{2\sigma}}I,$$

where μ_0 is the magnetic permeability and σ is the AC conductivity of the real metal, derived from the optical constants found in [17]. Equation (21) is thus still correct provided the matrix $\bar{\mathcal{Z}}$ is changed to $\bar{\mathcal{Z}} + dz_{\text{int}}\mathbb{I}_{N-2}$, with $z_{\text{int}} = \frac{1-j}{2\pi a}\sqrt{\frac{\mu_0\omega}{2\sigma}}$.

5. *Far-field calculation*

Once the axial current distribution along the antenna is known, we can calculate the scattered far-field. We approximate the far-field radiated by the antenna as the coherent sum of the fields radiated by a series of infinitesimal current elements distributed along the antenna and having amplitude and phase given by the current distribution solved for. We use an analytical expression for the radiation pattern of an infinitesimal electric dipole located on the plane interface between two dielectric half spaces (air and a medium of refractive index n)[18]. For the case of a dipole lying horizontally along the interface, the radiated field components in air are[18]:

$$\begin{aligned} E_\theta =& \kappa\Big[\tfrac{\cos^2\theta}{\cos\theta+(n^2-\sin^2\theta)^{1/2}} - \sin^2\theta\cos\theta \\ & \cdot \tfrac{\cos\theta-(n^2-\sin^2\theta)^{1/2}}{n^2\cos\theta+(n^2-\sin^2\theta)^{1/2}}\Big]\cos\phi\tfrac{e^{ik_0 r}}{r}, \\ E_\phi =& \quad -\kappa\tfrac{cos\theta sin\phi}{cos\theta+(n^2-\sin^2\theta)^{1/2}}\tfrac{e^{ik_0 r}}{r}, \end{aligned}$$

where the angles θ and ϕ are defined in Fig. 8.

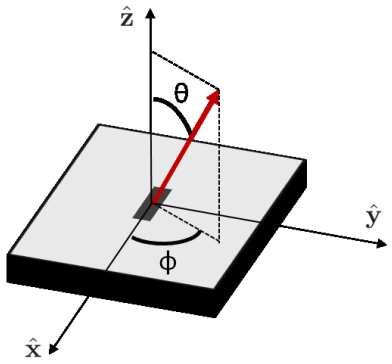

FIG. 8. Schematic of an infinitesimal horizontal electric dipole located at an interface between air ($z > 0$) and a dielectric medium ($z < 0$) of refractive index n.

6. *FDTD simulation details*

FDTD simulations realized using a commercial software (Lumerical FDTD) are used to validate our numerical solution. A realistic geometry is simulated, corresponding to fabricated V-shaped antennas[1]. Both arms have a rectangular cross-section, 200 nm wide and 100 nm thick. The antennas are defined on a silicon substrate. The interface between silicon and air lies at the center of the simulation area, which spans 4.5 μm x 4.5 μm x 6 μm (width x depth x height). Perfectly Matched Layers (PML) enclose the simulation area. The mesh cells are 30 nm x 30 nm x 15 nm in size in the plane of the antenna and within a 300 nm-thick layer encompassing the silicon-air interface (and the 100 nm-thick antenna itself). Beyond this layer, the vertical dimension of the mesh cells (height) is gradually increased to about 280 nm in air and 90 nm in silicon (or about $1/25^{th}$ of the wavelength in the medium). The simulation is stopped when an auto shutoff condition is reached corresponding to the fields in all cells being smaller than $10^{-5}E_0$,

where E_0 is the incident electric field amplitude. The time step is smaller than 0.037 fs. The optical constants are obtained by fitting the values found in Palik[17] to a multi-coefficient model.

We use a Total-Field Scattered-Field (TFSF) plane wave source encompassing the antenna. The dimensions of the total field region are 4.2 μm x 4.2 μm x 4 μm. The plane wave is launched in the direction perpendicular to the antenna, from the silicon side. A monitor is placed outside this region to isolate the scattered fields. A near-to far-field transform is then used to calculate the scattered field radiated in the direction perpendicular to the plane of the antenna.

[1] N. Yu, P. Genevet, M. A. Kats, F. Aieta, J.-P. Tetienne, F. Capasso and Z. Gaburro, Science **334**, 333 (2011).

[2] P. Genevet, N. Yu, F. Aieta, J. Lin, M. A. Kats, R. Blanchard, Z. Gaburro and F. Capasso, Appl. Phys. Lett. **100**, 13101 (2012).

[3] Y. Zhao and A. Alù, Phys. Rev. B, **84**, 205428 (2011).

[4] R. W. P. King, *The theory of linear antenna* (Harvard University Press, Cambridge, 1959).

[5] W. L. Stutzman and G. A. Thiele, *Antenna Theory and Design* (Wiley, New York, 1981).

[6] C. A. Balanis, *Antenna Theory, Analysis and Design* (Wiley, New York, 1982).

[7] S. J. Orfanidis, *Electromagnetic waves and antennas* (www.ece.rutgers.edu/ orfanidi/ewa).

[8] R. F. Harrington, IEEE Antennas and Propagation Mag. **32**, 31 (1990).

[9] R. F. Harrington, *Field Computation by Moment Methods* (Macmillan, New York, 1968).

[10] J. J. H. Wang, *Generalized Moment Methods in Electromagnetics* (John Wiley and Sons, New York, 1991).

[11] H. C. Pocklington, Proc. Cambridge Phil. Soc. (London, England) **9**, 324 (1897).

[12] N. Engheta, A. Salandrino and A. Alù, Phys. Rev. Lett. **95**, 095504 (2005).

[13] A. Alù and N. Engheta, Nat. Photonics **2**, 307 (2008).

[14] M. Staffaroni, J. Conway, S. Vedantam, J. Tang and E. Yablonovitch, Photonics Nanostruct. Fundam. Appl. **10**, 166 (2011).

[15] H. Nakano, Comput. Phys. Commun. **68**, 441 (1991).

[16] I. E. Rana and N. G. Alexopoulos, IEEE Trans. Antennas Propagat. **29**, 99 (1981).

[17] E. D. Palik, *Handbook of Optical Constants of Solids* (Academic press, 1991).

[18] N. Engheta, C. H. Papas and C. Elachi, Radio Sci. **17**, 1557 (1982).

[19] L. Novotny, N. van Hulst, Nat. Photonics **5**, 83 (2011).

[20] J. D. Jackson, *Classical Electrodynamics, Third edition* (John Wiley and Sons, Inc., 1998).

[21] D. H. Werner, P. L. Werner and J. K. Breakall, IEEE Trans. Antennas Propagat. **42**, 561 (1994).

[22] J. H. Richmond, Proc. IEEE **53**, 796 (1965).